# Supporting Information

## MOF-derived Bimetallic Core-shell Catalyst HZSM-5@$ZrO_2$-$In_2O_3$: High $CO_2$ Conversion in Reverse Water Gas Shift Reaction

Huimin Fang,[a] Guofeng Zhao,*[c] Denghui Cheng,[a] Jichang Liu,*[a b] Dengpeng Lan,[c] Qi Jiang,[a] Xuqiang Liu,[a] Jianping Ge,[c] Zhenliang Xu[a] and Haitao Xu*[a]

[a] *School of Chemical Engineering, East China University of Science and Technology, Shanghai 200237, China.*

[b] *Key Laboratory for Green Processing of Chemical Engineering of Xinjiang Bingtuan, School of Chemistry and Chemical Engineering, Shihezi University, Shihezi 832003, China.*

[c] *Shanghai Key Laboratory of Green Chemistry and Chemical Processes, School of Chemistry and Molecular Engineering, East China Normal University, Shanghai 200062, China.*

*To whom all correspondence should be addressed

E-mail address: liujc@ecust.edu.cn (Jichang Liu), gfzhao@chem.ecnu.edu.cn (Guofeng Zhao), xuhaitao@ecust.edu.cn (Haitao Xu).

## Materials and methods

**Materials:** The following chemicals were used without further purification. Zirconium chloride ($ZrCl_4$, 98%), Polyvinylpyrrolidone (PVP, MW = 58000) and indium nitrate tetrahydrate ($In(NO_3)_3 \cdot 4H_2O$, 99.9%) were purchased from Shanghai Macklin Biochemical Technology Co., Ltd. Terephthalic acid ($H_2BDC$, > 99%) was purchased from TCI (Shanghai) Development Co., Ltd. N, N-dimethylformamide (DMF, > 99.5 wt%), ethanol (EtOH, > 99.7%), acetic acid ($CH_3COOH$, 99.5%), sodium aluminate ($NaAlO_2$, anhydrous, analytic reagent) and tetraethyl orthosilicate (TEOS, analytic reagent) were provided by Shanghai Titan Scientific Co., Ltd. Tetrapropylammonium hydroxide (TPAOH, 40 wt% aqueous solution) was produced by Beijing Yanfeng Technology Co., Ltd. Ammonium chloride ($NH_4Cl$, 99.5%) was provided from Shanghai Lingfeng Chemical Reagent Co., Ltd.

**UIO-66:** UIO-66 was synthesized according to the previous study.[1] 33.4 mg $ZrCl_4$ and 25 mg $H_2BDC$ were dissolved sequentially in 10 mL DMF. 0.1 g PVP was weighed into above solution and sonication. After solution clarification, injected 0.7 mL $CH_3COOH$. The mixture was transferred into a 30mL Teflon-lined autoclave and reacted at 120 °C for 24 h. Final product was collected by centrifugation, then washed twice with DMF and ethanol, respectively.

**HZSM-5:** The HZSM-5 was prepared according to previous literature.[2] 0.05 g $NaAlO_2$ was dissolved in 4mL deionized water, and added 4 mL 40 wt% aqueous TPAOH to above solution. The mixture was stirred vigorously at room temperature for 30 min., then 6.85 mL TEOS was injected drop by drop. During the dropwise addition, the

solution became gradually cloudy and the rotation speed could be appropriately increased to make solution evenly mixed. After that, the mixture was stirred at 80 °C for 60-70 min and then back to room temperature for another 24 h. Poured obtained sol-gel into a 30 mL Teflon-lined autoclave and reacted for 48 h at 180 °C. The product was collected by centrifuged (5000 rpm, 5 min) and washed by deionized water (9000 rpm, 9 min) until the pH was below 9. The washed sample was dried for 6-8 h at 120 °C and calcinated at 600 ℃ in air for 5 h. Final product was $Na^+$ type ZSM-5. Ion exchange was performed twice to replace $Na^+$ with $NH_4^+$ completely by adding 2.0 g product into 80 mL 1.0 M $NH_4Cl$ solution at 90 °C stirring for 12 h. Product after ion-exchanged was collected by centrifugation (5000 rpm, 5 min) and washed with deionized water three times (9000 rpm, 9 min). Then, the washed product was dried for 6-8 h at 120 °C and calcinated at 550 ℃ in air for 5 h. The purpose of calcination was to convert $NH^{3+}$ to $H^+$ to obtain final product HZSM-5.

**HZSM-5@UIO-66:** 4.7 mg (0.020 mmol) $ZrCl_4$ and 3.3 mg (0.020 mmol) $H_2BDC$ were completely dissolved in EtOH and DMF, respectively as solution A and solution B. Weighed 7 mg HZSM-5 into solution A, and then mix it with solution B by sonication. The mixture was transferred into a 30 mL Teflon-lined autoclave and reacted at 120°C for 17 h. Final product was collected by centrifugation (5000 rpm, 5 min), then washed twice with DMF and EtOH, respectively (8000 rpm, 5 min).

**HZSM-5@$ZrO_2$:** The prepared HZSM-5@UIO-66 was calcined at 500 ℃ for 3 h to obtain HZSM-5@$ZrO_2$.

**HZSM-5@$ZrO_2$-$In_2O_3$:** In a typical procedure, HZSM-5@$ZrO_2$-$In_2O_3$ (70 wt%) was

prepared by excess volume impregnation. 2.5 g $In(NO_3)_3 \cdot 4H_2O$ was dissolved in 120 mL EtOH. Subsequently, 0.4 g as-synthesized HZSM-5@UIO-66 was dispersed in above solution and stirred vigorously at room temperature for 24 h. After stirring, the product was centrifuged once (5000 rpm, 5 min) and dried for 4h at 60 ℃. The dried product was calcined at 500℃ for 3h to obtain HZSM-5@$ZrO_2$-$In_2O_3$. The mass of $In(NO_3)_3 \cdot 4H_2O$ required for different $In_2O_3$ loadings is as follows: HZSM-5@$ZrO_2$-$In_2O_3$ (20 wt%)-0.269 g; HZSM-5@$ZrO_2$-$In_2O_3$ (30 wt%)-0.459 g; HZSM-5@$ZrO_2$-$In_2O_3$ (50 wt%)-1.074 g.

**$In_2O_3$/HZSM-5:** $In_2O_3$/HZSM-5 (70 wt%) was prepared by excess volume impregnation. 2.5 g $In(NO_3)_3 \cdot 4H_2O$ was dissolved in 120 mL EtOH. Subsequently, 0.4 g as-synthesized HZSM-5 was dispersed in above solution and stirred vigorously at room temperature for 24 h. After stirring, the product was centrifuged once (5000 rpm, 5 min) and dried for 4h at 60 ℃. The dried product was calcined at 500 ℃ for 3h to obtain $In_2O_3$/HZSM-5. The mass of $In(NO_3)_3 \cdot 4H_2O$ required for different $In_2O_3$ loadings is as follows: $In_2O_3$/HZSM-5 (20 wt%)-0.269 g; $In_2O_3$/HZSM-5 (30 wt%)-0.459 g; $In_2O_3$/HZSM-5 (50 wt%)-1.074 g.

**$In_2O_3$+HZSM-5:** Pure $In_2O_3$ was obtained by calcination of $In(NO_3)_3 \cdot 4H_2O$ at 500 ℃ for 3 h. 0.17 g $In_2O_3$ and 0.13 g HZSM-5 were powder mixed to obtain catalyst $In_2O_3$+HZSM-5. (The mass of $In_2O_3$ and HZSM-5 were determined according to the ICP results of HZSM-5@$ZrO_2$-$In_2O_3$ (Table. S2))

**$ZrO_2$+HZSM-5:** The prepared UIO-66 was calcined at 500 ℃ for 3 h to obtain pure $ZrO_2$. 0.17 g $ZrO_2$ and 0.13 g HZSM-5 were powder mixed to obtain catalyst

$ZrO_2$+HZSM-5. (The mass of $ZrO_2$ and HZSM-5 were determined according to the ICP results of HZSM-5@$ZrO_2$-$In_2O_3$ (Table. S2))

**$ZrO_2$-$In_2O_3$+HZSM-5:** 2.5 g $In(NO_3)_3 \cdot 4H_2O$ was dissolved in 120 mL EtOH. Subsequently, 0.4 g as-synthesized UIO-66 was dispersed in above solution and stirred at room temperature for 24 h. After stirring, the product was centrifuged once (5000 rpm, 5 min) and dried for 4h at 60 ℃. The dried product was calcined at 500℃ for 3h to obtain $ZrO_2$-$In_2O_3$. 0.17 g $ZrO_2$-$In_2O_3$ and 0.13 g HZSM-5 were powder mixed to obtain catalyst $ZrO_2$-$In_2O_3$+HZSM-5. (The mass of $ZrO_2$-$In_2O_3$ and HZSM-5 were determined according to the ICP results of HZSM-5@$ZrO_2$-$In_2O_3$ (Table. S2))

**Catalytic characterization**

High resolution transmission electron microscopy (HRTEM), high-angle annular dark-field scanning transmission electron microscopy (HAADF-STEM) imaging, and both correlating energy dispersive X-ray (EDX) elemental mappings were performed on JEM-2100 and JEM-2100 F at 200 kV, respectively. Powder X-ray diffraction (PXRD) dates were collected by Bruker AXS RINT 2000 Rigaku with Cu-Kα radiation in the 2θ range of 5-80°. After pretreatment, the $N_2$ adsorption-desorption curves of the samples were measured at 77K, and the specific surface area and pore size distributions were calculated using Brunauer-Emmett-Teller (BET) and Barrett-Joyner-Halenda (BJH) methods, respectively. The valence distribution of different elements was determined by X-ray photoelectron spectrometer (XPS) using ESCALAB 250Xi. The contents of In and Zr were determined by inductively coupled plasma emission spectrometer (Agilent 725 ICP-OES). Fourier transform infrared spectroscopy (FT-IR) spectra of the prepared samples were obtained using Nicolet 6700 Spectrometer.

**Catalyst evaluation**

In this paper, a continuous flow high pressure fixed-bed reactor was used to evaluate the performance of catalysts. The reactor is equipped with temperature controller (AI-516), mass flow controller (D08-1F), precision pressure gauge (YB-150A) and other related accessories to control the reaction temperature, flow, and pressure.

Usually, the prepared catalyst was pressed into powder in an agate mortar and loaded into a stainless steel reactor with an inner diameter of 8 mm. Before the reaction, pure Ar was introduced for 1h activation at 3 MPa and 400 ℃ with a flow rate of 30mL/min. After the reactor temperature cooled naturally to room temperature, the mixture of $H_2$:$CO_2$:Ar with a ratio of 73:24:3 was injected at a flow rate of 30 mL/min under 0.1 MPa, 2 MPa, 3 MPa and 4 MPa, respectively. Ar was used as the internal standard gas. Then, the reactor temperature was successively raised from room temperature to 280, 300, 320, 360, 380 and 400 ℃ (usually 400 ℃) and the sampling results were analyzed after the temperature had maintained for 10 min. Two sets of data were taken for each temperature to reduce errors. In addition, the influence of the change of space velocity (GHSV) on the reaction was also investigated by changing GHSV to 18000, 9000, 6000 and 4500 $mL \cdot h^{-1} \cdot g_{cat}^{-1}$.

In order to prevent liquid condensation, the gas outlet of the reactor was equipped with a section of insulated pipe connected with a gas chromatography (GC7900) for on-line analysis and detection. The GC-7900 was equipped with two chromatographic columns, one packed column TDX-1 connected to a thermal conductivity detector (TCD) for the detection of Ar, $CO_2$, CO and $CH_4$. Another capillary string, JN-PONA,

was connected to a hydrogen flame ion detector (FID) for the detection of $CH_3OH$ and other hydrocarbons. The $CO_2$ conversion, CO selectivity and $CH_3OH$ selectivity were calculated based on the mole number of carbon atoms, and the calculation formula is as follows.

$$CO_2\ Conversion = \frac{CO_{2\ inlet} - CO_{2\ outlet}}{CO_{2\ inlet}} \times 100\%$$

$$CO\ Selectivity = \frac{CO_{\ outlet}}{CO_{2\ inlet} - CO_{2\ outlet}} \times 100\%$$

$$CH_4\ Selectivity = \frac{CH_{4\ outlet}}{CO_{2\ inlet} - CO_{2\ outlet}} \times 100\%$$

$$CH_3OH\ Selectivity = \frac{CH_3OH_{\ outlet}}{CO_{2\ inlet} - CO_{2\ outlet}} \times 100\%$$

$CO_{2\ inlet}$ and $CO_{2\ outlet}$ represent the molar amount of $CO_2$ at the inlet and outlet, respectively; $CO_{\ outlet}$, $CH_{4\ outlet}$ and $CH_3OH_{\ outlet}$, respectively represent the moles of CO, $CH_4$ and $CH_3OH$ at the outlet.

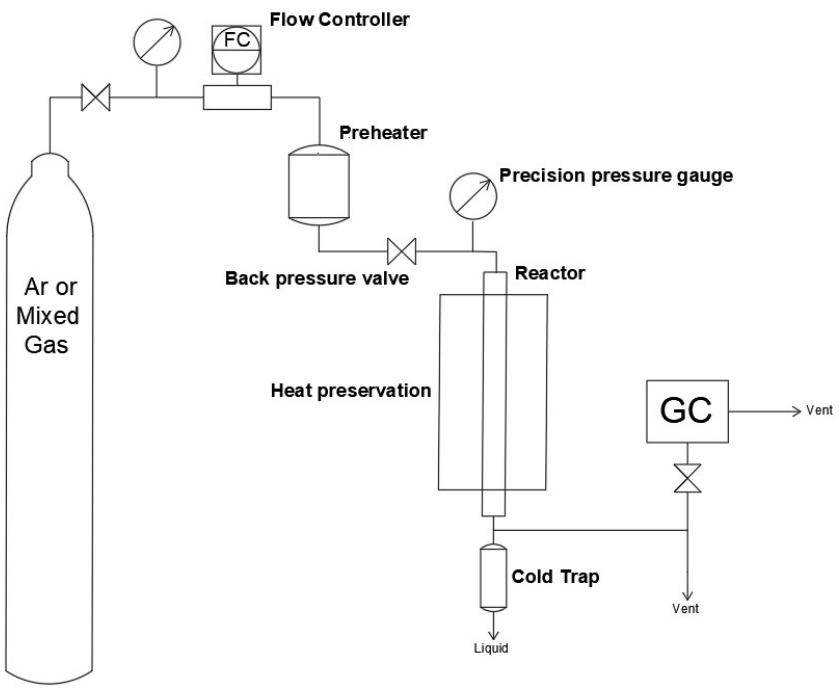


**Scheme S1.** Schematic flow diagram of the fixed bed reactor.

**Results and Discussion.**

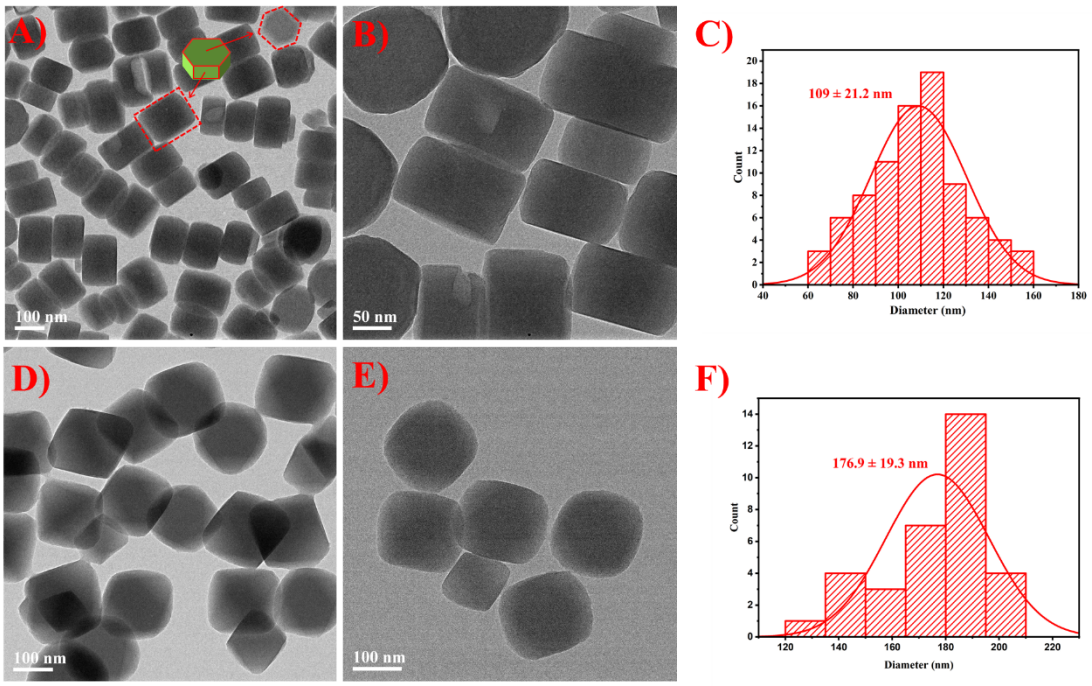


**Fig. S1.** (A, B) TEM images of as-synthesized HZSM-5 nanocrystals, (C) corresponding particle size histogram of HZSM-5 zeolites, (D, E) TEM images of as-synthesized UIO-66 nanocrystals, (F) corresponding particle size histogram of UIO-66.

As shown in Fig. S1A, B, the monodispersed HZSM-5 core (~110 nm) prepared was hexagonal with smooth surface and uniform size. As a core, it provided the surface on which UIO-66 could grow. The UIO-66 prepared was also nanoscale, but the size (~180 nm) was larger than HZSM-5, and the morphology was regular octahedral.

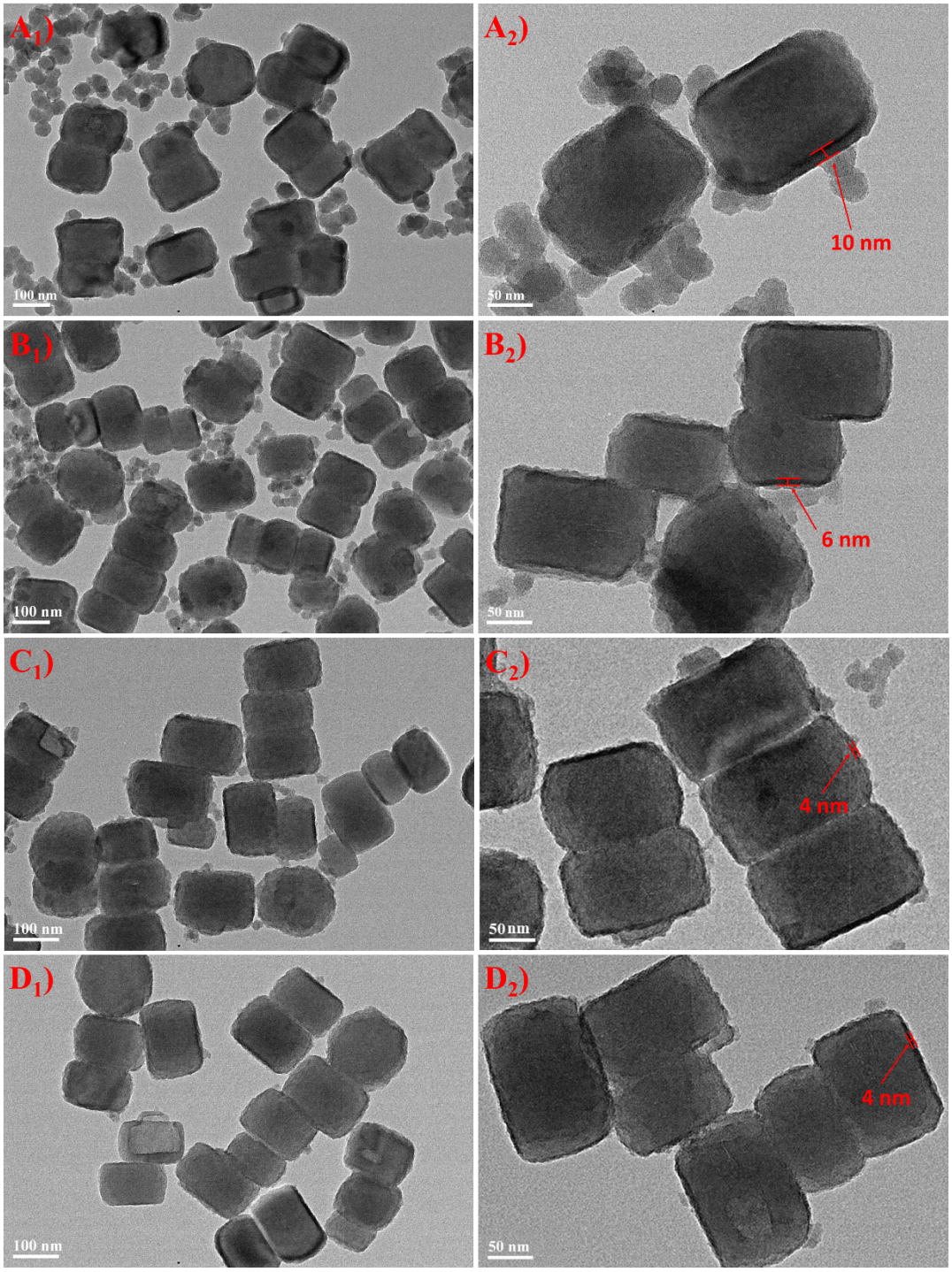


**Fig. S2.** $n(ZrCl_4) = n(H_2BDC)$ = ($A_1$, $A_2$) 0.035 mM, ($B_1$, $B_2$) 0.030 mM, ($C_1$, $C_2$) 0.025 mM, ($D_1$, $D_2$) 0.020 mM.

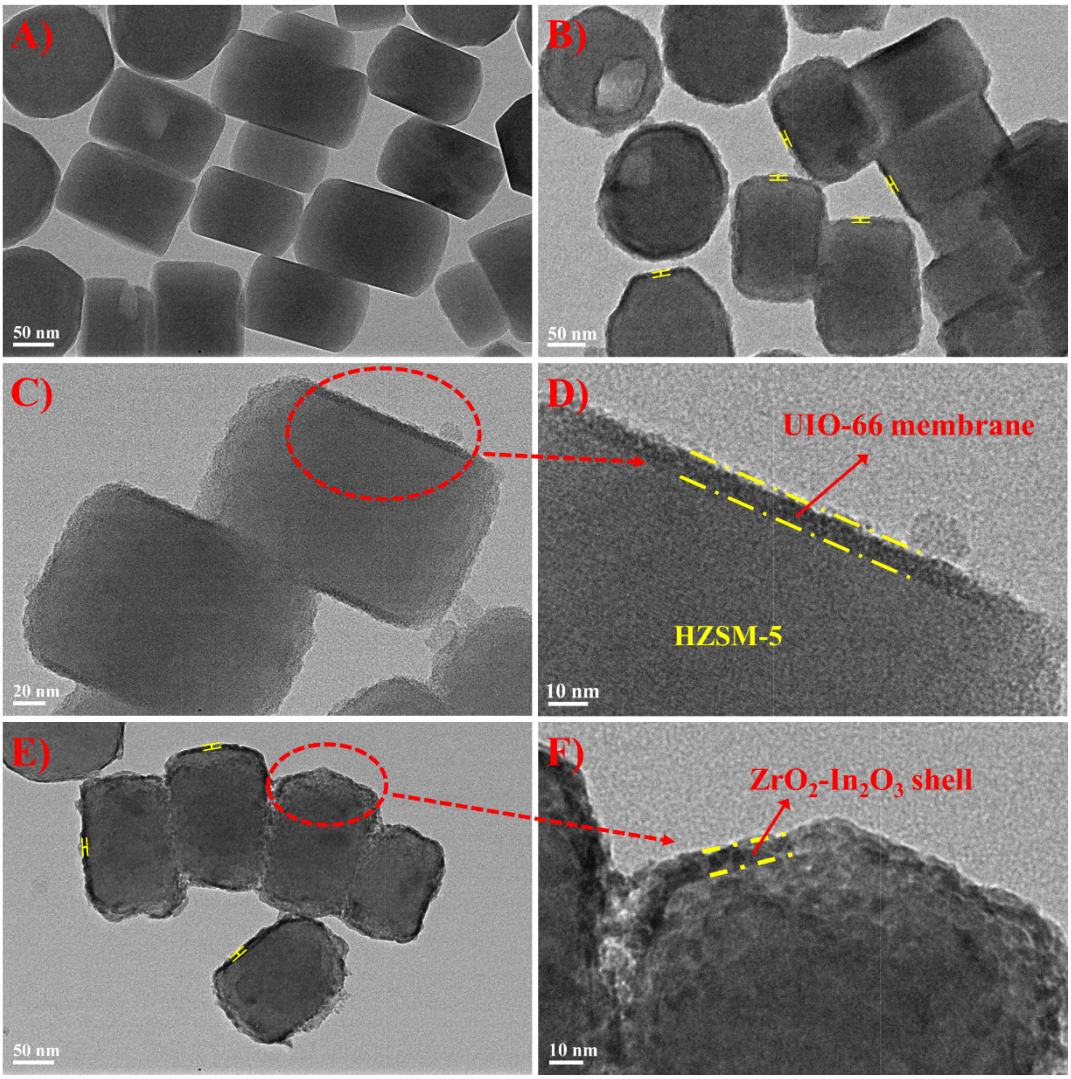


**Fig. S3.** TEM images of (A) HZSM-5, (B-D) HZSM-5@UIO-66, (E, F) HZSM-5@$ZrO_2$-$In_2O_3$.

As shown in Fig. S3, the HZSM-5 surface was smooth, while the HZSM-5@UIO-66 surface was rough with obvious membrane. In the enlarged view, a continuous UIO-66 membrane around the periphery of HZSM-5 was clearly seen. In Fig. S3E-F, HZSM-5@$ZrO_2$-$In_2O_3$ that obtained after impregnation and calcination still maintained the core-shell structure. The $ZrO_2$-$In_2O_3$ shell was also clearly seen in the enlarged view.

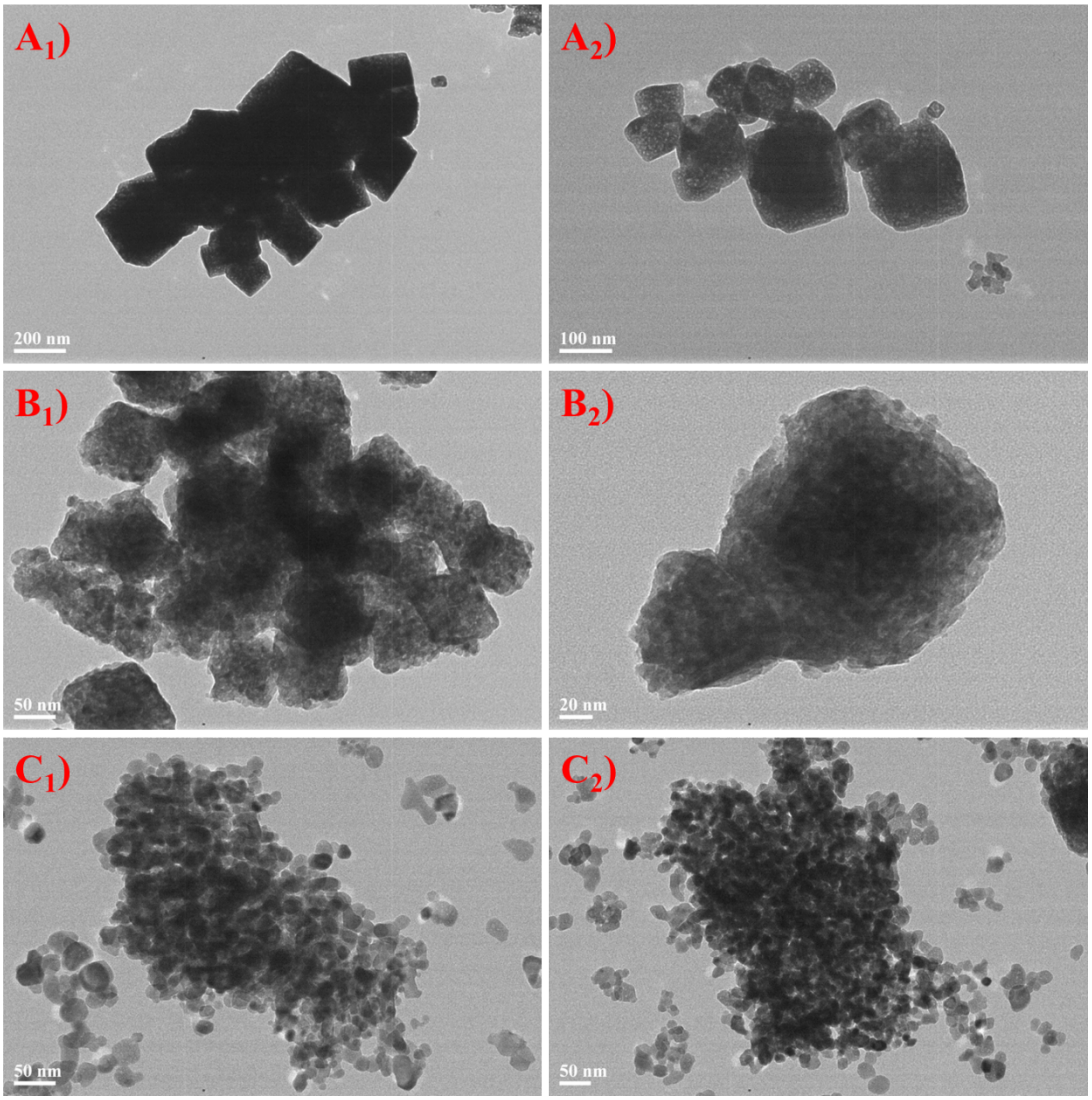


**Fig. S4.** TEM images of ($A_1$, $A_2$) pure $In_2O_3$, ($B_1$, $B_2$) pure $ZrO_2$, ($C_1$, $C_2$) $ZrO_2$-$In_2O_3$.

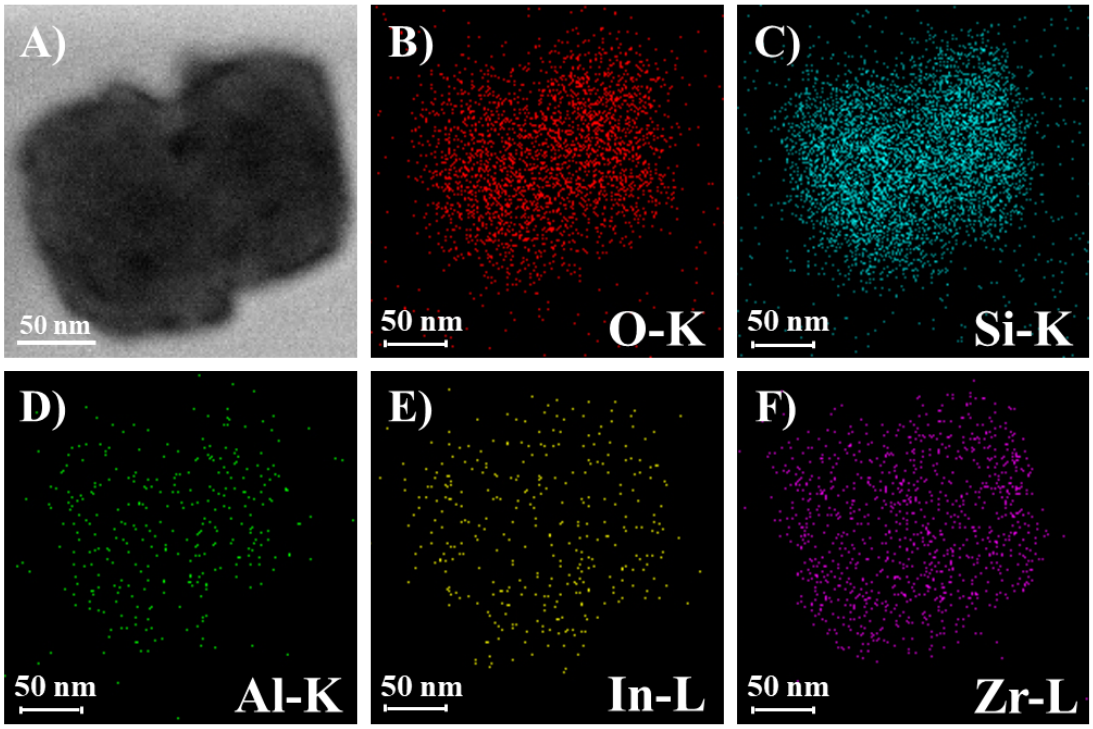


**Fig. S5.** (A) TEM image of HZSM-5@$ZrO_2$-$In_2O_3$(30 wt%), (B-F) EDX elemental mappings of the selected region.

In Fig.S5, Si, Al, O, Zr also existed in HZSM-5@$ZrO_2$-$In_2O_3$, and the presence of In element indicated that $In_2O_3$ was successfully loaded in impregnation. Although there was no obvious oxide shell as distinct as Fig. 3 in Fig. S5 due to the limitation of characterization instrument (ordinary High Resolution Transmission Electron Microscopy (HRTEM, JEM-2100)), it proved the presence of elements Zr and In in HZSM-5@$ZrO_2$-$In_2O_3$. Since HZSM-5@$ZrO_2$-$In_2O_3$ was derived from the core-shell material HZSM-5@UIO-66, and the TEM images of HZSM-5@$ZrO_2$-$In_2O_3$ also clearly showed the core-shell structure in Fig. S3E-F, thus the oxide obtained after impregnation and calcination was still anchored to the surface of HZSM-5 in the form of shell.

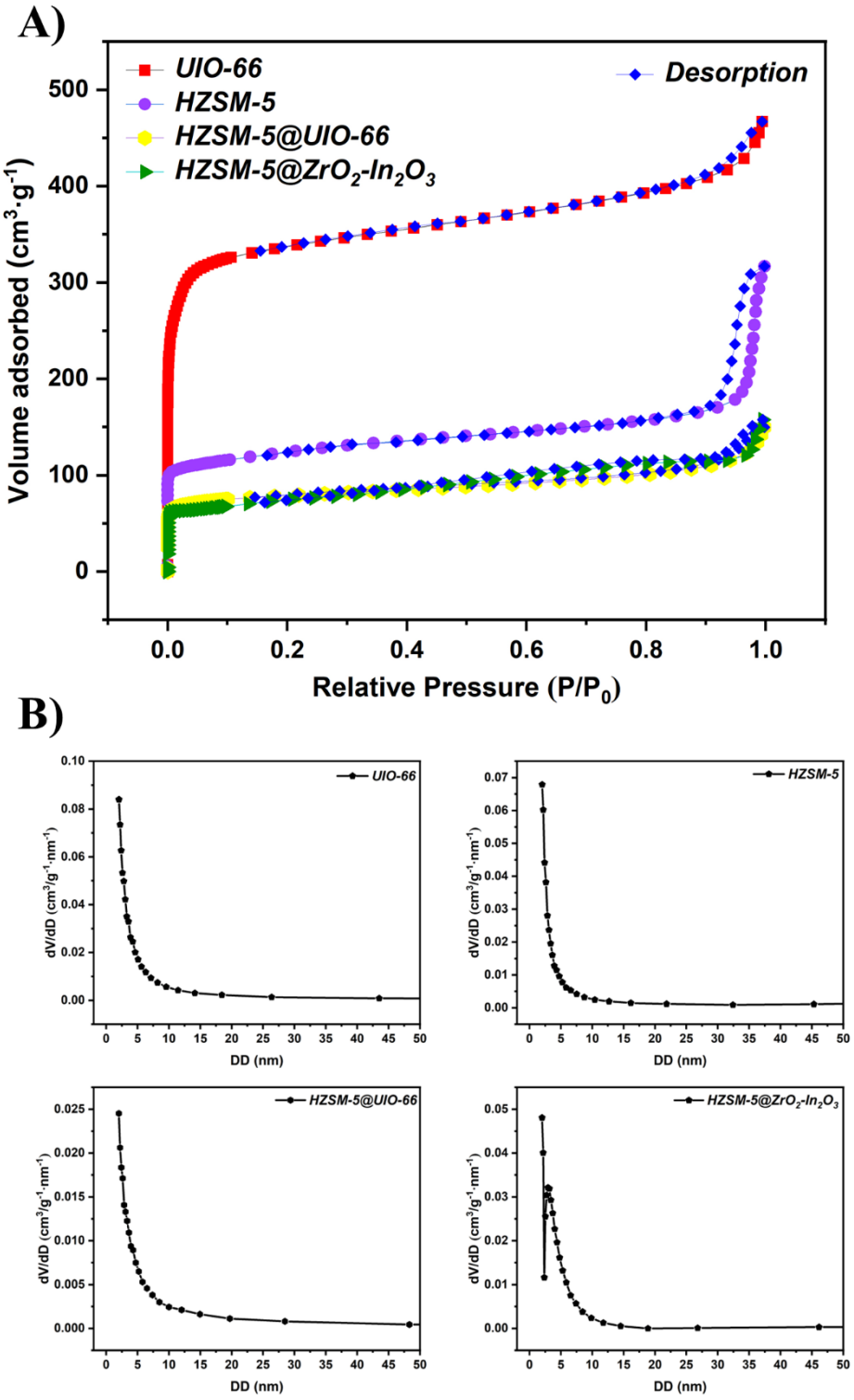


**Fig. S6.** (A) $N_2$ adsorption-desorption isotherms of different samples, (B) the corresponding pore size distributions.

Fig. S6A shows the $N_2$ adsorption-desorption isotherms for the four main materials.

When $P/P_0 < 0.1$, the adsorption capacity increases rapidly and tends to saturation due to the pore structure being filled with $N_2$. When relative pressure $P/P_0 > 0.1$, the adsorption capacity rises slowly and a plateau appears. The adsorption and desorption curves coincide and no desorption hysteresis occurs. All four materials showed typical type-I curves, indicating that four materials were microporous.

The images of pore size distribution were shown in Fig. S6B, and the highest point of four materials were all below 2 nm, indicating that all samples were mainly microporous. But HZSM-5@$ZrO_2$-$In_2O_3$ contained some mesopores, which was due to the oxidative decomposition reaction of organic linkers in UIO-66 membrane with oxygen during calcination. The disappearance of organic linkers generated some extra space in derivative, leading to the formation of mesopores.[3,4]

| Catalysts | BET surface area ($m^2 \cdot g^{-1}$) |
|---|---|
| UIO-66 | 1307.238 |
| HZSM-5 | 456.272 |
| HZSM-5@UIO-66 | 295.962 |
| HZSM-5@$ZrO_2$-$In_2O_3$ | 309.435 |

**Table S1.** Brunauer-Emmett-Teller (BET) surface area for the catalysts.

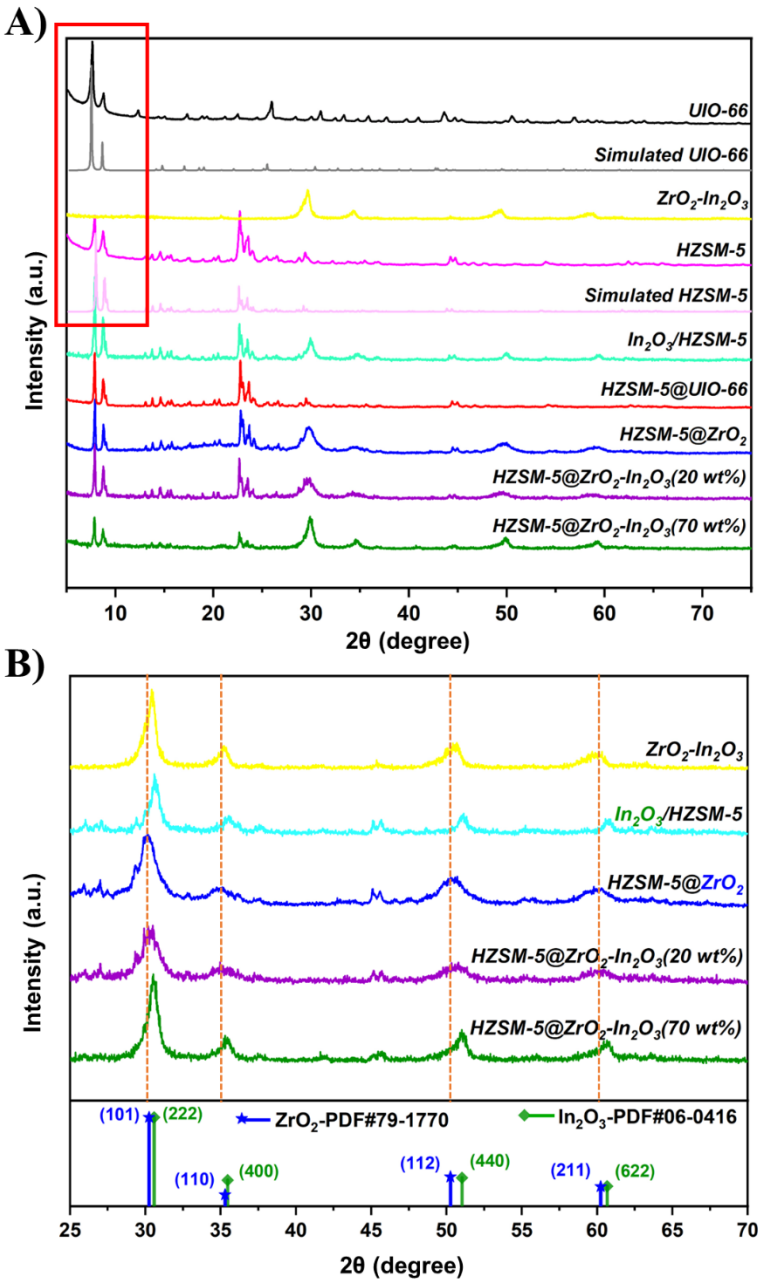


**Fig. S7.** (A) Powder X-ray diffraction patterns of different samples, (B) Magnified local XRD patterns of different samples.

The simulated PXRD patterns of UIO-66 and HZSM-5 were showed in Fig. S7A. By comparison, the PXRD patterns of UIO-66 and HZSM-5 matched their corresponding simulated patterns, indicating the successful synthesis of UIO-66 and HZSM-5. In addition, the UIO-66 and HZSM-5 prepared in this study are also consistent with PXRD patterns

reported in previous literatures.[2,5-7] But the characteristic diffraction peaks of UIO-66 and HZSM-5 were relatively close that difficult to distinguish, and the content of UIO-66 in the material was low. Therefore, the characteristic diffraction peaks of UIO-66 could not be clearly observed in PXRD pattern of HZSM-5@UIO-66.

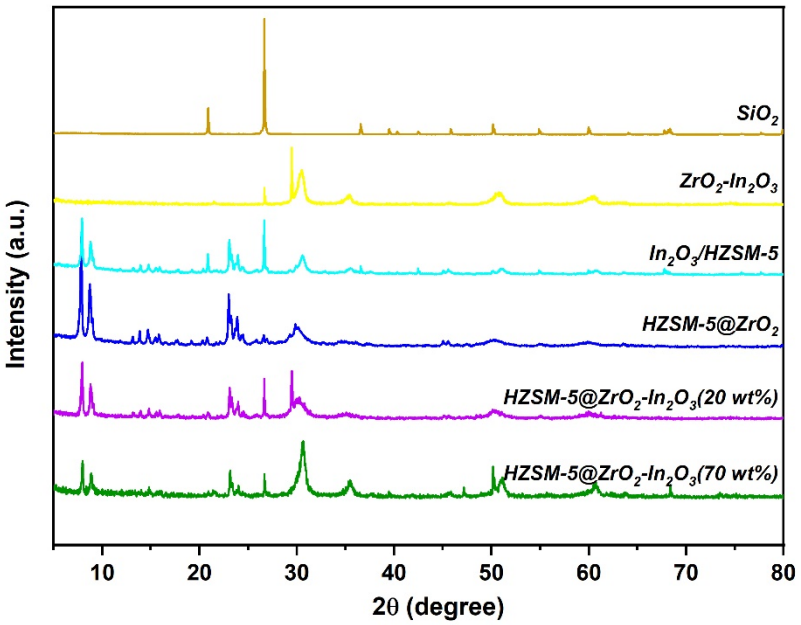


**Fig. S8.** XRD patterns of samples after RWGS reaction.

Fig. S8 shows the XRD patterns of five catalysts after reaction. Because some fine quartz sand could not be removed after catalysis, the XRD patterns of $SiO_2$ were also provided at the top of the figure. There was no significant difference between materials after reaction at 400 ℃, indicating that the thermal stability of several catalysts was outstanding.

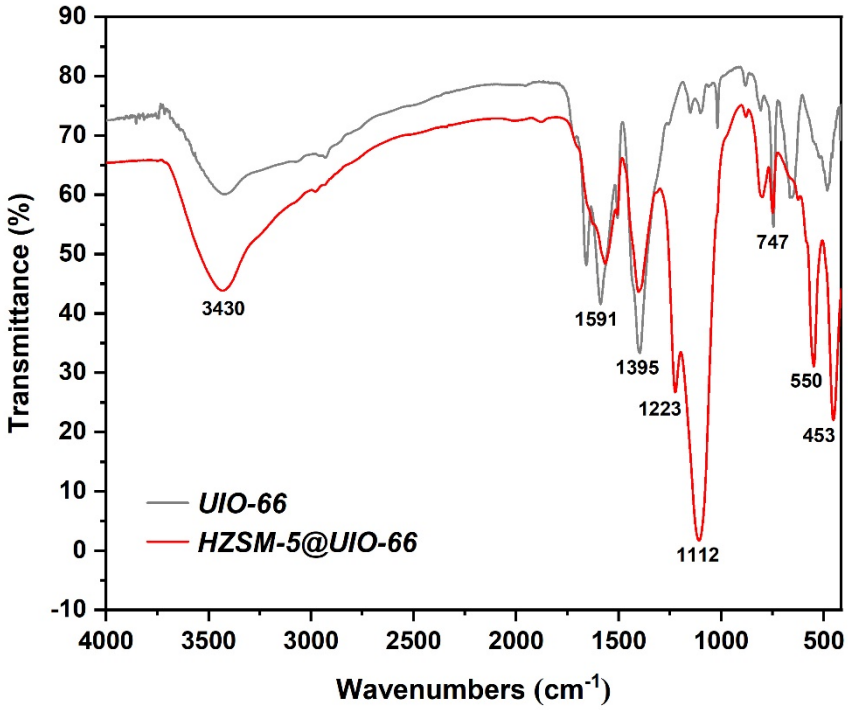


**Fig. S9.** Infrared spectra of UIO-66 and HZSM-5@UIO-66.

Fig. S9 compared the Infrared spectra of UIO-66 and HZSM-5@UIO-66. The peak at 3430 $cm^{-1}$ was the stretch frequency of O-H. At 1591 $cm^{-1}$, the peak that OCO asymmetric stretching of the carboxylate group in $H_2BDC$ occurred. The peak at 1395 $cm^{-1}$ was C-OH bond of carboxylic acid in $H_2BDC$.[6] 1223 and 1112 $cm^{-1}$ were the external and internal asymmetric stretching vibrations of $SiO_4$ or $AlO_4$ tetrahedron in HZSM-5 core, respectively.[8] Thus, they only existed in HZSM-5@UIO-66 sample. The peak at 747 $cm^{-1}$ should be C-H bending vibration peak of UIO-66. 550 and 453 $cm^{-1}$ were the skeleton vibration peak and T-O-T bending vibration peak in zeolite, respectively.[9] The Infrared spectra of UIO-66 and HZSM-5@UIO-66 had overlapping bands at 1591, 1395 and 747 $cm^{-1}$, confirming the existence of UIO-66 membrane in HZSM-5@UIO-66.

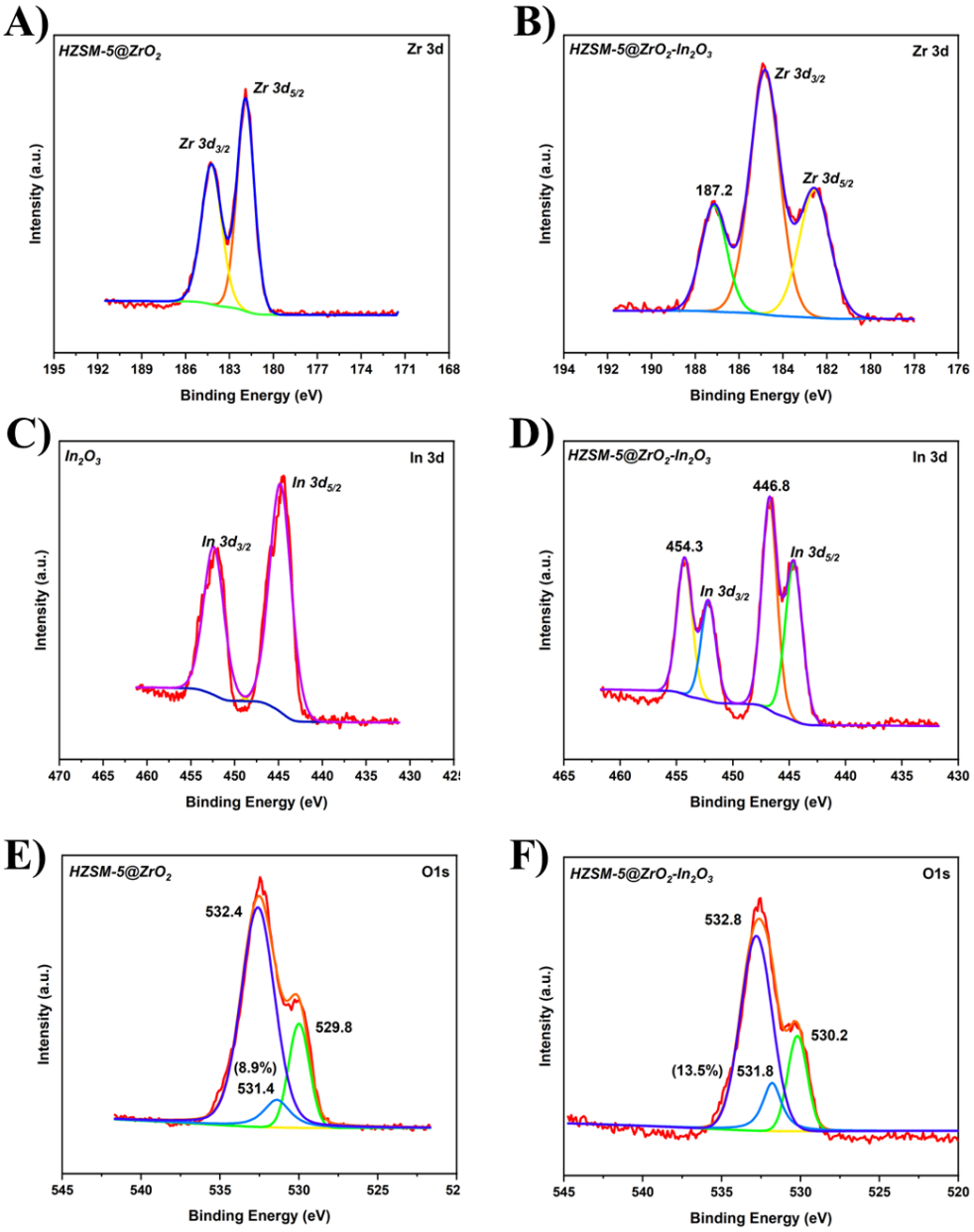


**Fig. S10.** XPS patterns of (A, E) HZSM-5@$ZrO_2$, (B, D, F) HZSM-5@$ZrO_2$-$In_2O_3$, (C) Pure $In_2O_3$.

The double peaks at 184.0 and 182.0 eV corresponded to Zr $3d_{3/2}$ and Zr $3d_{5/2}$, respectively (Fig. S10A), indicating the presence of $Zr^{4+}$ in the material.[10] However, compared with pure $ZrO_2$, HZSM-5@$ZrO_2$-$In_2O_3$ presented a new peak at a higher binding energy of 187.1 eV. It was attributed to the fact that part of In was incorporated

into $ZrO_2$ lattice to form In-O-Zr bond,[11] which changed the coordination states of part of Zr element. In 3d spectrum of pure $In_2O_3$ was shown in Fig. S10C. The two peaks at 452.4 and 444.8 eV represented In $3d_{3/2}$ and In $3d_{5/2}$, respectively, indicating the existence of $In^{3+}$,[10] while the In 3d spectrum of HZSM-5@$ZrO_2$-$In_2O_3$ also showed two new peaks at higher binding energy. It indicated that the coordination environment of In also be changed. Three peaks in O1s corresponded to lattice oxygen (~530 eV), oxygen vacancies (~531 eV) and O species in zeolites (~532 eV), respectively. HZSM-5@$ZrO_2$-$In_2O_3$ exhibited a higher concentration of oxygen vacancies than HZSM-5@$ZrO_2$, indicating that the combination of indium and zirconium generated more oxygen vacancies. Because the doping of In into the $ZrO_2$ lattice can leads to charge imbalance, and for charge balance, cations are squeezed out to form more oxygen vacancies.[11]

| Catalysts | $In_2O_3$ (wt%) Theoretical loading | $In_2O_3$ (wt%) Actual loading | $ZrO_2$ (wt%) Actual loading |
|---|---|---|---|
| $In_2O_3$/HZSM-5 | 70 | 19.2 | 0 |
| HZSM-5@$ZrO_2$-$In_2O_3$ | 70 | 31.0 | 26.1 |

**Table S2.** The actual loading of $In_2O_3$ and $ZrO_2$ in different composites were determined by inductively coupled Plasma Optical Emission Spectrometer (ICP-OES).

| Catalyst | T (℃) | P (MPa) | $H_2/CO_2$ | Con. (%) | Sel. (%) | Ref. |
|---|---|---|---|---|---|---|
| $In_2O_3$ | 400 | 0.1 | 1:1 | 6.18 | / | [12] |
| $Ga_2O_3$ | 400 | 0.1 | 1:1 | 2.99 | / | [12] |
| $In_2O_3/CeO_2$ | 400 | 0.1 | 1:1 | 5.34 | ~100 | [13] |
| $In_2O_3/ZrO_2$ | 400 | 2 | 3:1 | 23 | ~99 | [14] |
| Fe-Mo/$Al_2O_3$ | 400 | 0.1 | 1:1 | 5 | 100 | [15] |
| Cu-Ni/γ-$Al_2O_3$ | 600 | 0.1 | 1:1 | 28.7 | 79.7 | [16] |
| 10%Pd/$Al_2O_3$ | 400 | / | 3:1 | 35 | 11 | [17] |
| Pt/mullite | 400 | 0.1 | 1:1 | ~5 | 95.1 | [18] |
| HZSM-5@$ZrO_2$-$In_2O_3$ | 400 | 3 | 3:1 | 31.1 | 96.3 | This work |
| HZSM-5@$ZrO_2$-$In_2O_3$ | 400 | 0.1 | 3:1 | 14.5 | ~100 | This work |

**Table S3.** Performance comparison of different catalysts in RWGS reaction.

## References


1. H. Xu, X. Luo, J. Wang, Y. Su, X. Zhao and Y. Li, Spherical Sandwich Au@Pd@UIO-67/Pt@UIO-n (n = 66, 67, 69) Core–Shell Catalysts: Zr-Based Metal–Organic Frameworks for Effectively Regulating the Reverse Water–Gas Shift Reaction, *ACS Appl. Mater. Interfaces*, 2019, **11**, 20291-20297.
2. Z. Wan, W. Wu, G. Li, C. Wang, H. Yang and D. Zhang, Effect of $SiO_2/Al_2O_3$ ratio on the performance of nanocrystal ZSM-5 zeolite catalysts in methanol to gasoline conversion, *Appl. Catal. A: Gen.*, 2016, **523**, 312-320.
3. J. Liu, Y. He, L. Yan, K. Li, C. Zhang, H. Xiang, X. Wen and Y. Li, Nano-sized $ZrO_2$ derived from metal–organic frameworks and their catalytic performance for aromatic synthesis from syngas, *Catal. Sci. Technol.*, 2019, **9**, 2982-2992.
4. G. Qu, P. Jia, T. Zhang, Z. Li, C. Chen and Y. Zhao, UiO-66(Zr)-derived t-zirconia with abundant lattice defect for remarkably enhanced arsenic removal, *Chemosphere*, 2022, **288**, 132594.
5. J. H. Cavka, S. Jakobsen, U. Olsbye, N. Guillou, C. Lamberti, S. Bordiga and K. P. Lillerud, A New Zirconium Inorganic Building Brick Forming Metal Organic Frameworks with Exceptional Stability, *J. Am. Chem. Soc.*, 2008, **130**, 13850-13851.
6. N. Davoodian, A. Nakhaei Pour, M. Izadyar, A. Mohammadi and M. Vahidi, Fischer–Tropsch synthesis over a novel cobalt catalyst supported on UiO-66, *J. Iran Chem. Soc.*, 2021, **18**, 1043-1050.
7. Y. Xu, J. Wang, G. Ma, J. Lin and M. Ding, Designing of Hollow ZSM-5 with Controlled Mesopore Sizes To Boost Gasoline Production from Syngas, *ACS Sustain. Chem. Eng.*, 2019, **7**, 18125-18132.
8. S. Narayanan, J. J. Vijaya, S. Sivasanker, C. Ragupathi, T. M. Sankaranarayanan and L. J. Kennedy, Hierarchical ZSM-5 catalytic performance evaluated in the selective oxidation of styrene to benzaldehyde using TBHP, *J. Porous Mat.*, 2016, **23**, 741-752.
9. R. Sabarish and G. Unnikrishnan, Synthesis, characterization and catalytic activity of hierarchical ZSM-5 templated by carboxymethyl cellulose, *Powder Technol.*, 2017, **320**, 412-419.
10. M. M. Zain, M. Mohammadi, N. Kamiuchi and A. R. Mohamed, Development of highly selective $In_2O_3/ZrO_2$ catalyst for hydrogenation of $CO_2$ to methanol: An insight into the catalyst preparation method, *Korean J. Chem. Eng.*, 2020, **37**, 1680-1689.
11. Z. Zhang, Y. Huang, H. Ma, W. Qian, H. Zhang and W. Ying, Syngas-to-olefins over MOF-derived ZnZrOx and SAPO-34 bifunctional catalysts, *Catal. Commun.*, 2021, **152**, 106292.
12. Q. Sun, J. Ye, C.-j. Liu and Q. Ge, $In_2O_3$ as a promising catalyst for $CO_2$ utilization: A case study with reverse water gas shift over $In_2O_3$, *Greenhouse. Gas. Sci. Technol.*, 2014, **4**, 140-144.
13. W. Wang, Y. Zhang, Z. Wang, J.-m. Yan, Q. Ge and C.-j. Liu, Reverse water gas shift over $In_2O_3$–$CeO_2$ catalysts, *Catal. Today*, 2016, **259**, 402-408.

14. T. Numpilai, P. Kidkhunthod, C. K. Cheng, C. Wattanakit, M. Chareonpanich, J. Limtrakul and T. Witoon, CO2 hydrogenation to methanol at high reaction temperatures over $In_2O_3/ZrO_2$ catalysts: Influence of calcination temperatures of $ZrO_2$ support, *Catal. Today*, 2021, **375**, 298-306.
15. A. G. Kharaji, A. Shariati and M. A. Takassi, A Novel γ-Alumina Supported Fe-Mo Bimetallic Catalyst for Reverse Water Gas Shift Reaction, *Chin. J. Chem. Eng.*, 2013, **21**, 1007-1014.
16. Y. Liu and D. Liu, Study of bimetallic Cu–Ni/γ-$Al_2O_3$ catalysts for carbon dioxide hydrogenation, *Int. J. Hydrog. Energy*, 1999, **24**, 351-354.
17. J. H. Kwak, L. Kovarik and J. Szanyi, Heterogeneous Catalysis on Atomically Dispersed Supported Metals: $CO_2$ Reduction on Multifunctional Pd Catalysts, *ACS Catal.*, 2013, **3**, 2094-2100.
18. B. Liang, H. Duan, X. Su, X. Chen, Y. Huang, X. Chen, J. J. Delgado and T. Zhang, Promoting role of potassium in the reverse water gas shift reaction on Pt/mullite catalyst, *Catal. Today*, 2017, **281**, 319-326.